www.advsustainsys.com

Solar-Responsive Zr-MOF/Ag₄P₂O₇ Heterostructures for Sustainable Photocatalytic Degradation of Emerging Water Contaminants

Letícia G. da Trindade,* Antonio C. Roveda Jr., Marcelo Assis, Aline B. Trench, Yeison Núñez-de la Rosa, Luis Guillermo Cuadrado Durango, Carlos H. M. Fernandes, Juliana C. Barreiro, Márcio Daldin Teodoro, Moacir Rossi Forim, Lucia H. Mascaro, Elson Longo, Aryel Heitor Ferreira, Ivana Grčić, Daniel R. Cardoso, and Edson A. Ticianelli*

The rational design of heterostructured photocatalysts with engineered architectures is crucial for advancing sustainable energy-environmental technologies. Here, a microwave-assisted strategy is developed to construct a Zr-MOF/Ag₄P₂O₇ heterostructure, synergistically integrating the high surface area and robustness of zirconium-based-frameworks with the visible-light activity of silver pyrophosphate. The hybrid exhibits enhanced charge separation and solar photon harvesting, enabling efficient degradation of a broad range of organic dyes and fluoroquinolone antibiotics. The coexistence of hexagonal and orthorhombic Ag₄P₂O₇ phases is proposed to form internal phase junctions that enhance charge-carrier separation, contributing to the superior photocatalytic performance of the heterostructure. The optimized MOF/Ag-2 composition (Zr:Ag = 1:2) achieved removal efficiencies above 95% for multiple pollutants, supported by mechanistic insights from dynamic light scattering (DLS), zeta potential, and electron paramagnetic resonance (EPR) analyses, which identified •OH and h⁺ as the dominant reactive species. Advanced characterization, LC-MS monitoring, and phytotoxicity assays validated the transformation of contaminants into less harmful intermediates. Importantly, Six-Flux Modeling demonstrated that the heterostructure absorbs nearly seven times more visible photons than UVA, confirming its solar responsiveness. These findings highlight Zr-MOF/Ag₄P₂O₇ as a cost-effective and structurally engineered photocatalyst, offering a blueprint for the next generation of multifunctional materials tailored for sustainable environmental remediation and beyond.

1. Introduction

Water contamination by synthetic dyes and pharmaceuticals represents a growing environmental and public health concern. Dyes, widely employed across textile, food, cosmetic, and pharmaceutical industries, are often carcinogenic and bioaccumulative due to their stable aromatic structures, such as azobonded compounds, which pose significant risks to aquatic ecosystems and human health.[1-4]

More recently, increasing attention has turned to the environmental burden caused by antibiotics, particularly fluoroquinolones, which are widely used in both human and veterinary medicine. Residual antibiotics frequently enter water bodies through hospital, domestic, and agricultural runoff, contributing to ecological disruption and accelerating the global crisis of antimicrobial resistance. [5,6] Given their persistence and low biodegradability, removing these contaminants from water systems has become a critical objective.

Several physical, chemical, and biological treatment strategies have been

L. G. da Trindade, A. C. Roveda Jr., J. C. Barreiro, D. R. Cardoso, E. A. Ticianelli

São Carlos Institute of Chemistry University of São Paulo - USP São Carlos, SP 13560-970, Brazil

E-mail: lg.trindade@unifesp.br; edsont@iqsc.usp.br

The ORCID identification number(s) for the author(s) of this article can be found under https://doi.org/10.1002/adsu.202501297

© 2025 The Author(s). Advanced Sustainable Systems published by Wiley-VCH GmbH. This is an open access article under the terms of the Creative Commons Attribution License, which permits use, distribution and reproduction in any medium, provided the original work is properly cited.

DOI: 10.1002/adsu.202501297

L. G. da Trindade, A. H. Ferreira Mackenzie Institute for Research in Graphene and Nanotechnologies -MackGraphe Mackenzie Presbyterian University

São Paulo, SP 01302-907, Brazil

M. Assis
Department of Biosciences
Federal University of São Paulo (UNIFESP)
Santos, SP 11015-020, Brazil

A. B. Trench, Y. Núñez-de la Rosa, C. H. M. Fernandes, L. H. Mascaro, E. Longo

Department of Chemistry Universidade Federal de São Carlos - UFSCar São Carlos, SP 13565-905, Brazil

www.advsustainsys.com

explored to tackle this issue.^[6-9] Among them, semiconductorbased photocatalysis stands out for its efficiency, costeffectiveness, and potential use of solar energy. This method relies on light-induced generation of reactive species, such as hydroxyl and superoxide radicals, which drive the oxidation and breakdown of complex pollutants into harmless byproducts.[10]

Traditional photocatalysts like TiO₂, [11,12] ZnO, [13,14] and Ag-based materials^[15,16] have demonstrated effectiveness but face limitations under visible-light conditions. Notably, silverbased semiconductors offer enhanced charge transfer, tunable bandgaps, and inherent antimicrobial activity, making them highly suitable for environmental applications.[17-20]

Metal-organic frameworks (MOFs), with their crystalline porous architectures composed of metal clusters and organic linkers, have emerged as a new class of photocatalysts. [21,22] Their large surface areas, tunable porosity, and functionalizable frameworks offer unique advantages. However, pure MOFs often suffer from low quantum efficiency and rapid recombination of photogenerated charge carriers. [23,24] A compelling strategy to overcome these limitations is to couple MOFs with light-responsive semiconductors, thereby forming heterostructures that improve charge separation and photon utilization.

Among MOFs, zirconium-based frameworks (Zr-MOFs) are particularly appealing due to their superior chemical and thermal stability, as well as structural integrity in aqueous environments.[25-28] Several studies have demonstrated enhanced photocatalytic activity in Zr-MOF-based composites. For instance, Ding et al.[23] reported a UiO-66(Zr)/Bi₂MoO₆ composite with significantly improved Rhodamine B degradation under visible-light. Similarly, Wang et al.^[29] developed NiIn₂S₄/UiO-66 composites capable of degrading tetracycline with near-complete efficiency within 90 min, highlighting the synergistic effects of MOF - semiconductor combinations.

Silver-based metal-organic framework (Ag-MOF) composites have been increasingly exploited to address the intrinsic limitations of pristine MOFs, namely low quantum efficiency and rapid electron-hole recombination.[30,31] By incorporating Ag nanoparticles, nanoclusters or ionic silver species into MOF matrices, these composites enhance visible-light absorption, act as electron sinks or plasmonic enhancers, and thus substan-

A. B. Trench Centro de Ciências Naturais e Humanas Universidade Federal do ABC – UFABC Santo André, SP 09210-170, Brazil Y. Núñez-de la Rosa

Faculty of Engineering and Basic Sciences Fundación Universitaria Los Libertadores Bogotá 111221, Colombia

L. G. C. Durango, M. R. Forim Postgraduate Program in Biotechnology Universidade Federal de São Carlos - UFSCar São Carlos, SP 13565-905, Brazil

M. D. Teodoro Department of Physics Federal University of São Carlos São Carlos, SP 13565-905, Brazil

University of Zagreb Faculty of Geotechnical Engineering Hallerova aleja 7, Varaždin 42000, Croatia

tially improve overall photocatalytic performance. [32,33] A key example is the work by Arenas-Vivo et al., [32] who developed an ultrafast, reproducible photoreduction strategy to prepare an Ag-nanocluster@MIL-125-NH2 composite that exhibited superior visible-light photocatalytic activity for the degradation of both dye (methylene blue) and antibiotic (sulfamethazine) in batch and continuous-flow systems. Likewise, Zheng et al.[34] synthesized a ternary UiO-66(Ce)/Ag/BiOBr heterocomposite exhibiting 93.5% photocatalytic oxidation of ketoprofen after 180 min under visible-light, where the combined plasmonic effect, Ce4+/Ce3+ redox cycling, and Schottky junction promoted efficient electron transfer and reactive oxygen species generation. Similarly, Liu et al. developed an AgBr/AgCl@ZIF-8 photocatalyst capable of removing ≈98% of Rhodamine B (RhB) under visible irradiation.^[35] Collectively, these studies confirm that embedding Ag species into MOF architectures is a robust route to suppress charge-carrier recombination, extend visible-light response, and accelerate the photocatalytic elimination of persistent organic pollutants (including antibiotics) from aqueous ma-

Building on these concepts, the present study introduces a novel Zr-MOF/ Ag₄P₂O₇ heterostructure, synthesized through a microwave-assisted solvothermal route, to address the dual challenge of dye and antibiotic contamination. The integration of Zr-MOF and Ag₄P₂O₇ yields a multifunctional photocatalyst with optimized visible-light responsiveness, surface charge, and pollutant affinity.

The photocatalytic activity of the synthesized materials was systematically investigated using model pollutants: Rhodamine B (RhB), Methylene Blue (MB), Methyl Orange (MO), and two fluoroquinolone antibiotics ciprofloxacin (CIP) and enrofloxacin (ENR). Degradation efficiency was evaluated alongside LC-MS and phytotoxicity assays to assess breakdown pathways and residual toxicity.

A particularly novel aspect of this study is the application of Six-Flux Modeling (SFM)[36–38] to elucidate the optical absorption and scattering behavior of the Zr-MOF/Ag-2 composite. This modeling approach provided quantitative insights into its photon capture capabilities and correlated them directly with photocatalytic outcomes.

Altogether, the findings offer a compelling case for the design of next-generation photocatalysts based on MOF-semiconductor heterostructures, specifically tailored for real-world wastewater treatment applications.

2. Results and Discussion

2.1. Structural Characterization

The XRD patterns of the pure samples of Zr-MOF and $Ag_4P_2O_7$, and of MOF/Ag-05, MOF/Ag-1, and MOF/Ag-2 composites are shown in Figure 1a. The Zr-MOF diffraction pattern is in good agreement with the previously reported data, indicating that the sample has been successfully synthesized. [23,39] The analysis of the diffraction pattern of this sample shows that the material has two Ag₄P₂O₇ phases, being hexagonal (JCPDS No.37-0187)^[40] and orthorhombic (JCPDS No. 40-058).[41] The orthorhombic phase is the major phase in the sample, since the most intense peaks in the XRD pattern are related to this phase. The

onlinelibrary.wiley.com/doi/10.1002/adsu.202501297 by University Of Sao Paulo - Brazil, Wiley Online Library on [24/11/2025]. See the Terms.

conditions) on Wiley Online Library for rules of use; OA articles are governed by the applicable Creative Commons

(a)

ntensity (a.u.)

Zr-MOF

Ag,P,O,

MOF/Ag-05

MOF/Ag-1 MOF/Ag-2

20

(c)

Ag, P,O, • orthorhombic

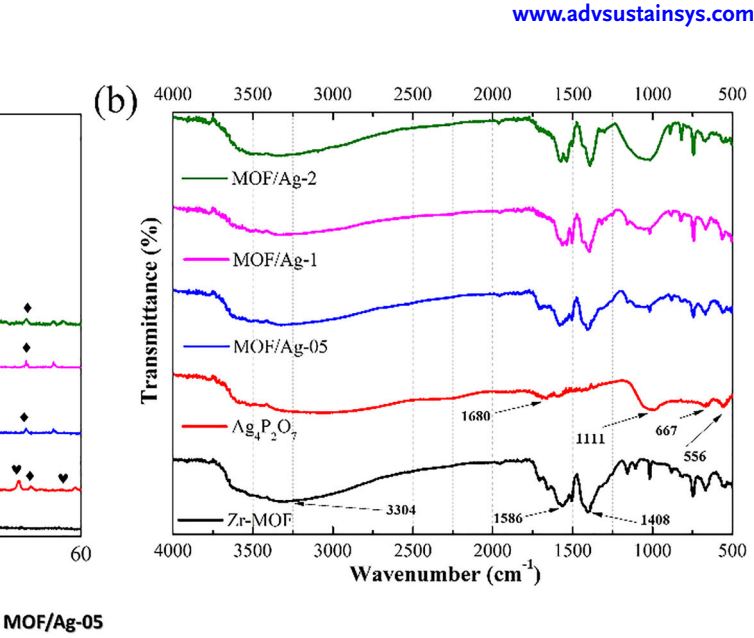
30

20 (degree)

50

Zr-BDC 4

hexagonal



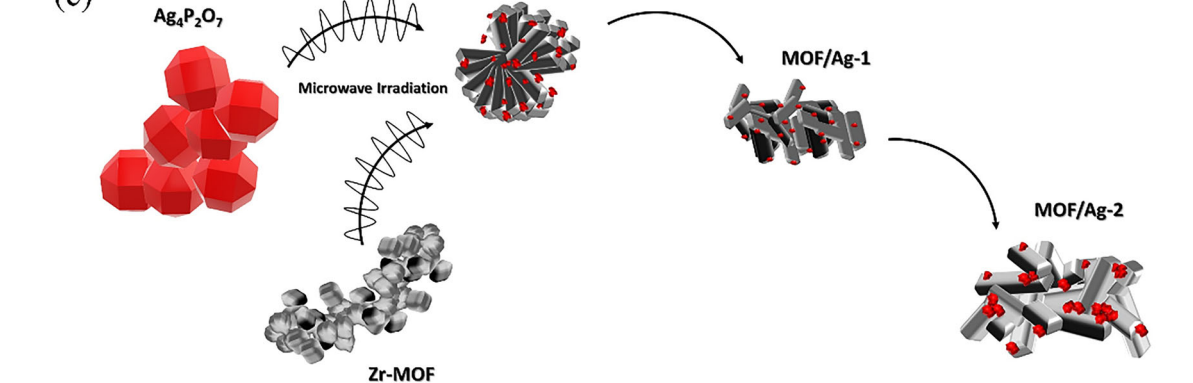


Figure 1. a) XRD patterns and b) FT-IR of Zr-MOF, Ag₄P₂O₇, MOF/Ag05, MOF/Ag-1, and MOF/Ag-2 samples. c) schematic representation of the morphology changes of Zr-MOF/Ag₄P₂O₇ heterostructures.

diffraction peaks for each phase are identified and shown in Figure 1a. After the incorporation of Ag₄P₂O₇, the peaks belonging to the Zr-MOF structure can still be observed in all modified samples (MOF/Ag-05, MOF/Ag-1, and MOF/Ag-2), indicating that the crystal structure of the Zr-MOF is maintained during the synthesis of the composite material. It is observed that when increasing the amounts of Ag₄P₂O₇, the diffraction peaks referring to the Zr-MOF have their relative intensities decreased, while the peaks referring to the Ag₄P₂O₇ sample have their intensities highlighted, indicating the heterostructure formation. This result shows that the MOF/Ag samples were successfully synthesized, since the Ag₄P₂O₇ and Zr-MOF phases appear in both samples. An interesting fact to observe is that in samples MOF/Ag-05 and MOF/Ag-1, there is a considerable decrease in the hexagonal phase of $Ag_4P_2O_7$. In this way, Zr-MOF can work as a phase driver for Ag₄P₂O₇. This effect is totally dependent on the concentration of Zr-MOF, since in MOF/Ag-2 there is the formation of unidentified by-products, and the equivalent turn of both phases of Ag₄P₂O₇.

FT-IR spectra of all samples are shown in Figure 1b. Characteristic bands of Zr-MOF are observed at 1408 and 1586 cm⁻¹, in agreement with previous work.^[42] The Ag₄P₂O₇ spectrum shows bands at 556, 667, and 1111 cm⁻¹ that can be attributed to the fundamental vibrational bands of pyrophosphates that are observed at frequencies varying from 500 to 1280 cm⁻¹.[41,42] The O-P-O bending vibration v_4 is represented by a band in 556 cm⁻¹, whereas the band in 667 cm⁻¹ is related to symmetric $v_{1(s)}$ P-O-P vibrational modes and the band in 1111 cm⁻¹ is assigned to symmetric stretching mode of P-O bonds in PO₄ tetrahedra. [43-45] The 1680 cm⁻¹ band found in the Ag₄P₂O₇ spectrum and the 3304 cm⁻¹ band found in all samples are described as O-H bending and O-H asymmetry stretching modes of water molecules adsorbed on the surface of the samples.^[46] When Zr-MOF/Ag₄P₂O₇ samples are considered, it is observed that the bands related to Zr-MOF and Ag₄P₂O₇ are still present. Although some bands can no longer be distinguished because they are observed in the same region of the spectrum, the peak at ≈ 1111 cm⁻¹ relative to the symmetric stretching mode of P-O bonds can be observed in the Zr-MOF/Ag₄P₂O₇, and its relative intensity increases with an increase in Ag₄P₂O₇ content in the sample. In summary, the XRD and FT-IR analysis confirm that the heterostructures were successfully synthesized.

Figure 1c illustrates the synthesis of the MOF/Ag composites. Zr-MOF and Ag₄P₂O₇ are combined under microwave





www.advsustainsys.com

irradiation to form MOF/Ag-05, MOF/Ag-1, and MOF/Ag-2. The schematic helps visualize the gradual increase of Ag₄P₂O₇ content and its effect on the composite structure, as observed in the XRD results. It also highlights the role of Zr-MOF in preserving its structure and directing the phase transformation of Ag₄P₂O₇. The reduction of the hexagonal phase in MOF/Ag-05 and MOF/Ag-1, and the appearance of by-products in MOF/Ag-2, are consistent with the diffraction data.

The coexistence of hexagonal and orthorhombic Ag₄P₂O₇ phases observed in the XRD patterns (Figure 1a) is particularly relevant to the photocatalytic behavior of the heterostructure. Several studies have reported that the junction between different crystalline phases of the same semiconductor can act as an internal interface that promotes charge-carrier separation and suppresses electron-hole recombination, enhancing photocatalytic activity through built-in electric fields and defectmediated pathways. [47-49] In the case of Ag₄P₂O₇, the coexistence of both phases has been associated with complementary band structures and distinct electronic densities, facilitating charge transfer across the phase boundary.[47] Pereira et al.[47] and Promnopas et al.[48] demonstrated that Ag₄P₂O₇-based materials exhibiting mixed phases or coupled with Ag₃PO₄ display superior performance under visible-light compared with single-phase counterparts. These effects have been attributed to phase-junction-induced electron migration and increased density of surface-active sites.^[40,49,50] Therefore, the dual-phase character of Ag₄P₂O₇ in our Zr-MOF/Ag₄P₂O₇ composite likely contributes synergistically to the observed high activity by facilitating interfacial charge transport and reactive oxygen species formation.

Figure 2 presents the morphological characterization of all synthesized samples, as observed by field-emission scanning electron microscopy (FE-SEM). The Zr-MOF exhibits irregular spherical particles with an average size of $\approx 0.25 \, \mu m$ (Figure 2Aa), a morphology characteristic of Zr-based metal-organic frameworks (MOFs).^[24] In contrast, the Ag₄P₂O₇ particles (Figure 2Ab) display a well-defined rhombic dodecahedral geometry with an average particle size of $\approx 5.9 \,\mu\text{m}$. [50] As corroborated by XRD analysis, Zr-MOF acts as a phase driver for Ag₄P₂O₇, significantly influencing the morphology of the resulting heterostructures. This morphological modulation is clearly evidenced in the MOF/Ag-05 sample (Figure 2Ac), wherein the Zr-MOF undergoes a notable transformation into hierarchical rod-like structures. These rods are decorated with small Ag₄P₂O₇ nanoparticles uniformly distributed on their surface. As the Ag₄P₂O₇ concentration increases, in the MOF/Ag-1 sample (Figure 2Ad), a partial loss of the hierarchical morphology is observed, leading to the formation of smaller Zr-MOF rods still decorated with Ag₄P₂O₇ nanoparticles. Further increasing the Ag₄P₂O₇ content, as seen in the MOF/Ag-2 sample (Figure 2Ae), results in a higher density of Zr-MOF rods accompanied by noticeable agglomeration of Ag₄P₂O₇ particles. Notably, the morphological and structural features of the synthesized Zr-MOF are consistent with a MIL-140-type framework. This assignment is supported by the presence of characteristic low-angle reflections in the XRD pattern (see Figure 1a) together with the rod-like particle morphology observed by SEM. [51–53] The formation of a MIL-140-type topology under our microwave-assisted, water-containing conditions is consistent with previous reports showing that modest water

Adv. Sustainable Syst. 2025, e01297

content and specific synthetic modulators favor rod-chain Zr-MOF crystallization.[54]

To further validate these observations, transmission electron microscopy (TEM) analysis was conducted on the MOF/Ag-2 sample (Figure 2Ba). Consistent with the XRD data, Zr-MOF lacks a well-defined crystalline structure, whereas the Ag₄P₂O₇ phase exhibits clear crystallinity. High-resolution TEM (HR-TEM) performed on the nanoparticles adhered to the Zr-MOF rods (Figure 2Bb,c) revealed an interplanar distance of 0.28 nm, corresponding to the (1112) crystallographic plane of hexagonal Ag₄P₂O₇, thereby corroborating the FE-SEM observations. Additionally, energy-dispersive X-ray spectroscopy (EDX) mapping (Figure 2Ca-f) confirms a homogeneous spatial distribution of C, Ag, Zr, O, and P elements across the entire sample. This indicates the successful formation of a well-integrated heterostructure, without significant phase segregation between Zr-MOF and Ag₄P₂O₇ components. The quantitative elemental composition is provided in Figure S2 (Supporting Information).

The morphological evolution from irregular Zr-MOF aggregates to hierarchical rod-like architectures in the Zr-MOF/Ag₄P₂O₇ composite can be attributed to a growthmodification mechanism induced by interfacial interactions and altered coordination environment. Introduction of Ag+ and phosphate during synthesis likely alters the surface energy and local chemical milieu around Zr4+ centers, triggering anisotropic crystal growth or oriented-attachment mechanisms that favors rodlike assembly rather than isotropic aggregation. Such morphological control by modulator ions, solvent/ion-mediated surface restructuring, and interfacial templating is well documented for Zr-MOFs^[53,55–58] and underpins the favorable charge separation and improved photocatalytic activity observed here.

After structural and morphological characterization, the hydrodynamic size and colloidal stability of Zr-MOF, Ag₄P₂O₇, and MOF/Ag-2 suspended particles were analyzed using DLS and zeta potential, respectively, **Table 1**.

Dynamic light scattering (DLS) analysis revealed distinct colloidal behaviors among the samples. The pristine Zr-MOF exhibited an apparent hydrodynamic diameter of 14.2 \pm 2 μm and a PDI of 39.2 %, indicative of a highly aggregated state in aqueous suspension. The Ag₄P₂O₇ sample displayed a smaller apparent size (8.8 \pm 6 μ m, PDI = 34.5 %), suggesting partial improvement in dispersion, whereas the MOF/Ag-2 heterocomposite exhibited the lowest hydrodynamic diameter (6.3 \pm 2 μ m) and PDI (24.9%), evidencing enhanced colloidal uniformity and stability. Zeta potential measurements corroborated this trend: Zr-MOF presented a positive surface potential of + 26.3 mV, while Ag₄P₂O₇ and MOF/Ag-2 exhibited negative values of -18.9 and -26.8 mV, respectively (Figure S3, Supporting Information). Although none surpassed the \pm 30 mV threshold typically associated with strong electrostatic stabilization, the shift toward more negative values in MOF/Ag-2 indicates improved repulsive interactions and reduced aggregation tendency. These colloidal findings are consistent with the morphological features observed by microscopy. SEM analyses (Figure 2A) revealed that pristine Zr-MOF consists of irregular spherical particles ($\approx 0.25 \,\mu\text{m}$), while the Ag₄P₂O₇ phase forms rhombic dodecahedral crystals (≈5.9 µm). In the MOF/Ag-2 heterocomposite, the Zr-MOF rods are densely decorated with Ag₄P₂O₇ nanoparticles, forming hierarchical rod-like architectures, as confirmed

) on Wiley Online Library for rules of use; OA articles are governed by the applicable Creative Commons

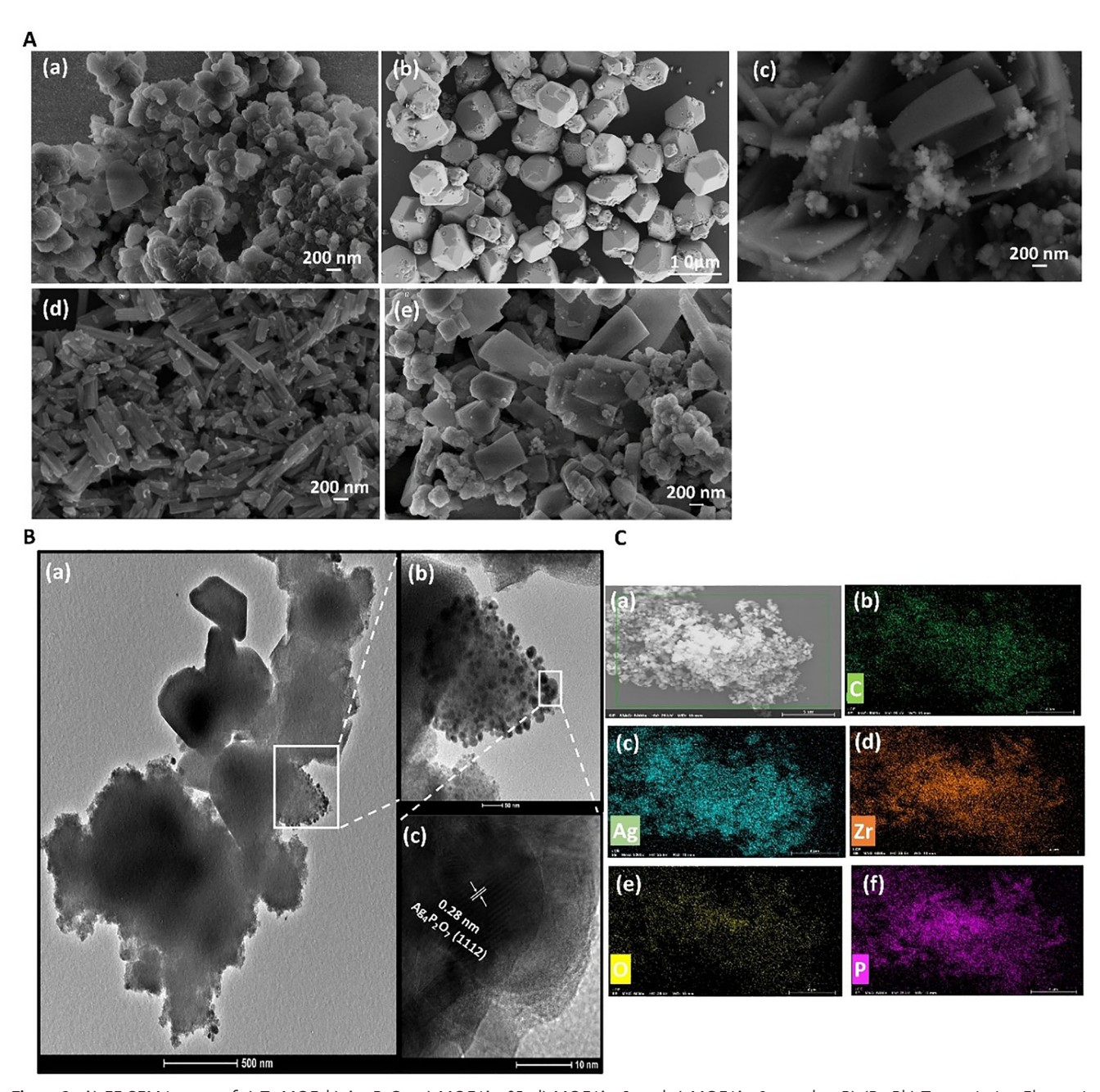


Figure 2. A) FE-SEM images of a) Zr-MOF, b) $Ag_4P_2O_7$, c) MOF/Ag-05, d) MOF/Ag-1, and e) MOF/Ag-2 samples. B) (Ba,Bb) Transmission Electronic Microscopy (TEM) of the MOF/Ag-2 sample. (Bc) HR-TEM image of $Ag_4P_2O_7$ particles on the MOF/Ag-2 sample. C) EDX mapping of the following elements, C, Ag, Zr, O, and P, of the MOF/Ag-2 sample.

Table 1. Hydrodynamic diameter, polydispersity index (PDI), zeta potential, and interpretation of colloidal stability for Zr-MOF, $Ag_4P_2O_7$, and the MOF/Ag heterocomposite in aqueous suspension.

Sample	Hydrodynamic diameter [μm]	Polydispersity index [%]	Potencial zeta [mV]	Interpretation of colloidal stability Moderate stability	
Zr-MOF	14.2 ± 2	39.2	+26.3 ± 1		
$Ag_4P_2O_7$	8.8 ± 6	34.5	-18.9 ± 1	Low stability	
MOF/Ag-2	6.3 ± 2	24.9	-26.8 ± 1	Moderate stability	



www.advsustainsys.com

by TEM (Figure 2B). The decrease in hydrodynamic diameter and polydispersity index, combined with the more negative zeta potential, demonstrates that the formation of the Zr-MOF/ Ag₄P₂O₇ heterostructure improves dispersion stability in aqueous media, a favorable characteristic for photocatalytic applications.

SEM analysis (Figure 2A) revealed that the pristine Zr-MOF, originally consisting of irregular spherical particles with an average diameter of ≈0.25 µm, transformed after Ag₄P₂O₇ deposition into hierarchical rod-like architectures. Based on the SEM images, the individual rods measure $\approx 0.8-1.0 \,\mu m$ in length and 0.25-0.30 µm in thickness. The evolution from isotropic to anisotropic morphology agrees with the DLS data, which show a reduced hydrodynamic diameter for the MOF/Ag-2 sample, reflecting decreased aggregation and enhanced colloidal dispersion. This morphological transformation is attributed to interfacial and anisotropic re-growth processes induced by Ag+ and phosphate ions, which modify the local coordination environment, surface energy, and nucleation kinetics of the MOF crystals. Similar phenomena, where secondary ions or modulators promote oriented attachment and the assembly of rod-like or hierarchical Zr-MOFs, have been widely reported in the literature. [56-59] These structural modifications occur without compromising the chemical integrity of the framework, as Zr-based MOFs are well known for their outstanding thermal and chemical stability owing to the strong Zr-O coordination bonds and the high connectivity of Zr₆O₄(OH)₄ clusters.[53,60] Therefore, the morphological evolution observed in the Zr-MOF/Ag₄P₂O₇ heterostructures results from ion-directed anisotropic growth rather than framework degradation, consistent with the intrinsic robustness of the Zr-MOF under the mild synthesis conditions employed.

2.2. Electronic Characterization

Adv. Sustainable Syst. 2025, e01297

To investigate charge carrier dynamics in the Zr-MOF/Ag₄P₂O₇ heterostructure, photoluminescence (PL) spectra were recorded (Figure 3a). Zr-MOF showed a strong emission at 474 nm, indicating rapid electron-hole recombination, while Ag₄P₂O₇ exhibited a peak at 532 nm, associated with intrinsic transitions. The heterostructures MOF/Ag-05 and MOF/Ag-2 displayed blueshifted peaks (452 and 459 nm) and significantly reduced PL intensities—especially with higher Ag₄P₂O₇ content, suggesting efficient interfacial charge separation.

These findings agree with the literature showing that heterojunctions and defect modulation in Zr-MOFs improve charge separation by altering the electronic structure. [61-63] The likely formation of a type-II band alignment between Zr-MOF and Ag₄P₂O₇ promotes spatial charge separation, reducing recombination.

Bandgap energies (E_a) were calculated via the Tauc method (Figure 3b). Zr-MOF showed an indirect E_{σ} of 3.72 eV;[23,64] Ag₄P₂O₇ had dual bandgaps at 3.67 and 1.83 eV, attributed to hexagonal and orthorhombic phases.^[45] MOF/Ag composites exhibited decreasing E_g values with increasing Ag₄P₂O₇: 3.84 eV (MOF/Ag-05), 3.68 eV (MOF/Ag-1), and 3.45 eV (MOF/Ag-2), likely due to changes in particle size, surface features, and defect states.[65]

2.3. Photocatalytic Activity

2.3.1. Photodegradation of RhB Dve

Rhodamine B (RhB) was selected as a model dye due to its well-characterized structure, strong visible absorbance, and high aqueous solubility, making it suitable for evaluating photocatalytic degradation and interfacial interactions. [66] The photocatalytic activity of all samples was assessed under visible-light following a 30 min dark adsorption-desorption equilibration. As shown in Figure 4a, after 1 h of irradiation, Zr-MOF and Ag₄P₂O₇ achieved 25% and 40% RhB degradation, respectively, while heterostructures MOF/Ag-05, MOF/Ag-1, and MOF/Ag-2 reached 64%, 69%, and 95%. This enhanced performance is attributed to the synergistic interaction between MOF and Ag₄P₂O₇.^[39]

The degradation kinetics followed pseudo-first-order behavior (Figure 4b), [67] as confirmed by regression analyses (zero-order: $k = 6.7 \times 10^{-8} \text{ min}^{-1}$; first-order: $k = 0.0364 \text{ min}^{-1}$; secondorder: $k = 2.6 \times 10^4 \text{ L mol}^{-1} \text{ s}^{-1}$; Figure S4, Supporting Information). The apparent rate constants (k, Figure S5, Supporting Information) followed the trend: MOF/Ag-2 > MOF/Ag-1 > $MOF/Ag-05 > Ag_4P_2O_7 > Zr-MOF$. Notably, MOF/Ag-2 showed k values eight- and five-fold higher than Zr-MOF and Ag₄P₂O₇, respectively, consistent with its reduced PL intensity (Figure 3a-e), indicative of suppressed charge recombination.[68]

Photocatalytic stability tests (Figure 4c) revealed slight activity loss from the first to the second cycle for MOF/Ag-2, followed by stable performance in the third, confirming reasonable recyclability.

For a better understanding of the photocatalytic mechanism involved in the degradation of the RhB dye, tests were carried out to capture reactive species that can participate in the degradation mechanism, using BQ, AO, and TBA to capture $O_2^{\bullet-}$, h^+ , and OH, respectively. The sample used for this experiment had the best photocatalytic response, which was MOF/Ag-2. Figure 4d shows the results obtained. It is noted that no changes were observed when adding BQ (100% degradation), indicating that the O2 •- radical did not participate in the RhB degradation mechanism. When adding AO, there was a decrease in degradation (27% degradation), indicating that the species h^+ may be the dominant species in the degradation process followed by the radical *OH, which also resulted in a decrease in degradation after TBA addition (77% degradation).

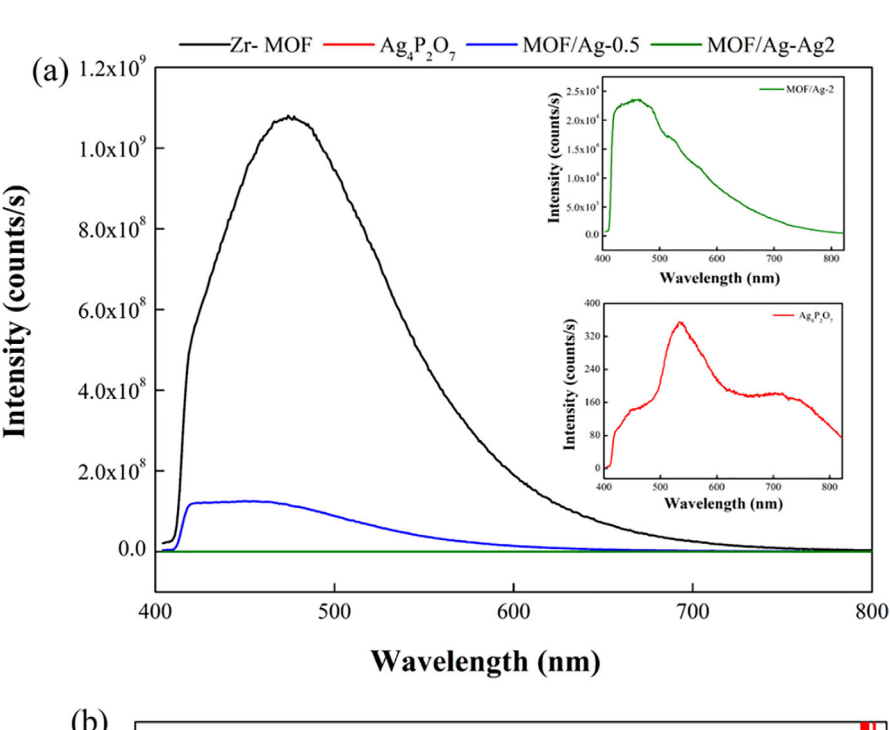
To further evaluate the effectiveness of the catalysts, the decrease in the total organic carbon (TOC) concentration during the photodegradation processes was also determined. Figure 4e shows the TOC removal efficiency of RhB in the degradation process by Zr-MOF, MOF/Ag-2, and the photolysis process (i.e., degradation without photocatalyst). As expected for the MOF/Ag-2 catalyst under visible radiation for 60 min, the TOC removal (≈48 %) was much higher than when the pure material Zr-MOF (\approx 24 %) and the photolysis process (\approx 2%), indicating that MOF/Ag-2 degrades and mineralizes RhB in a short time under visible-light irradiation. This finding may be explained by the main photogenerated species, h^+ and ${}^{\bullet}OH$ (Figure 4d), forming CO2, H2O, and COC (including intermediate compounds like short-chain carboxylic acids).

Concerning possible terminal oxidation intermediates, LC-UV-Vis analysis was performed to further investigate the

onlinelibrary.wiley.com/doi/10.1002/adsu.202501297 by University Of Sao Paulo

Brazil, Wiley Online Library on [24/11/2025]. See

on Wiley Online Library for rules of use; OA articles are governed by the applicable Creative Commons



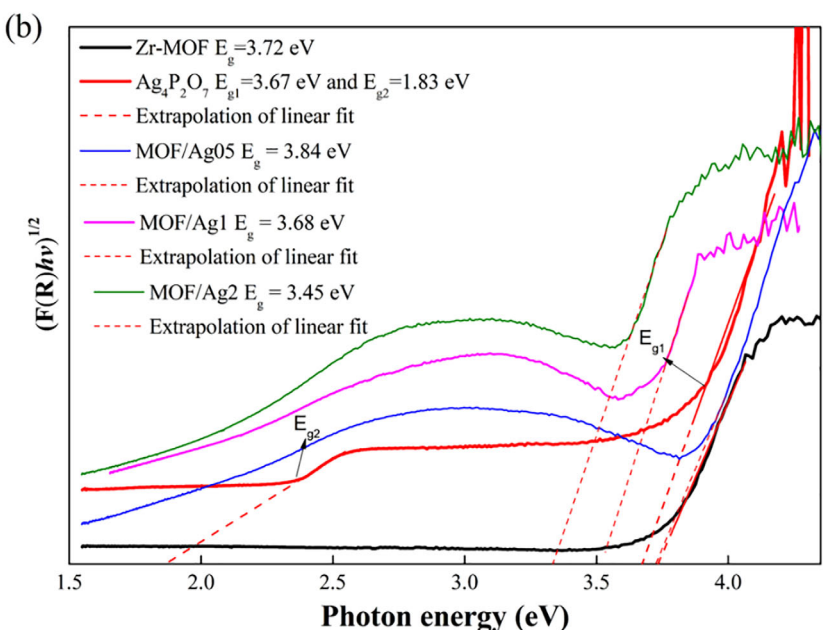
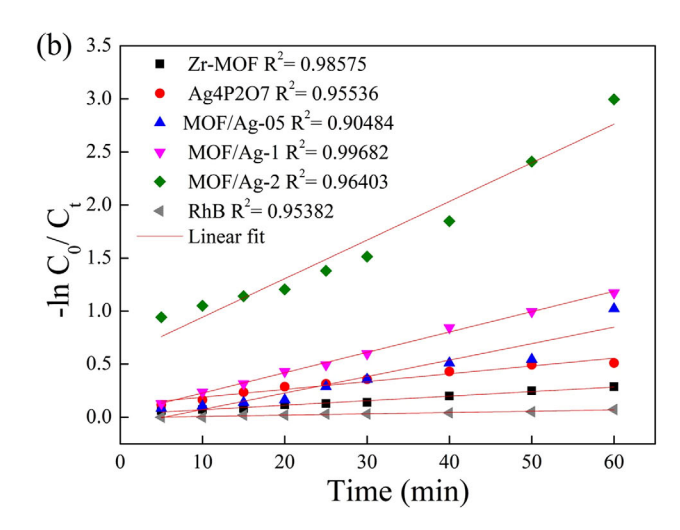


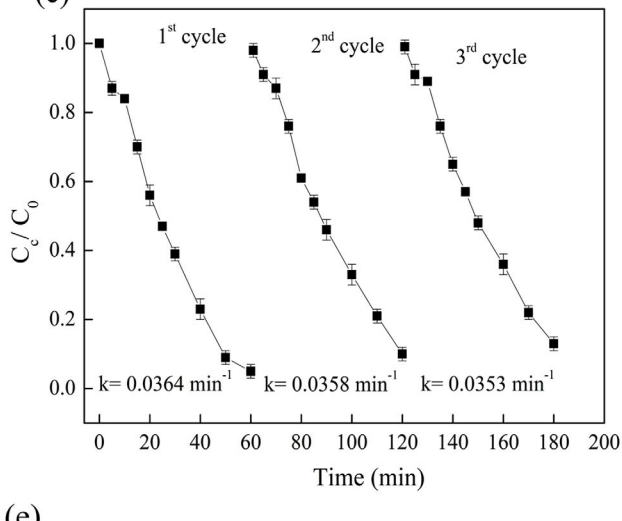
Figure 3. a) Photoluminescence (PL) spectra and b) Tauc plots of Zr-MOF, $Ag_4P_2O_7$, and MOF-Ag samples.

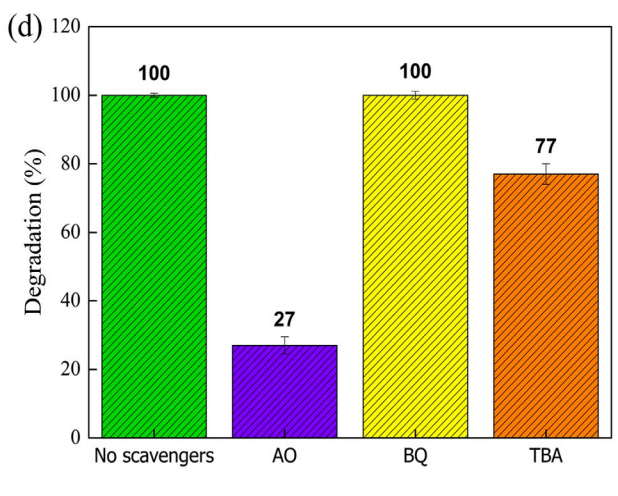
short-chain carboxylic acids produced in RhB degradation and mineralization. As expected, no carboxylic acids were detected during RhB degradation by pure Zr-MOF and the photolysis process. On the other hand, only five terminal oxidation intermediates were detected (although 20 standards were used), acetic, formic, glycolic, maleic, and succinic acids, when MOF/Ag-2 was used (see Figure 4f). The intermediate compounds formed are similar to those previously reported for the literature in the degradation of RhB by the Fenton and photocatalysis processes.^[69–71] As reported by Wang, et al., ^[69] these compounds could be produced during RhB oxidation. Briefly, the RhB is first degraded

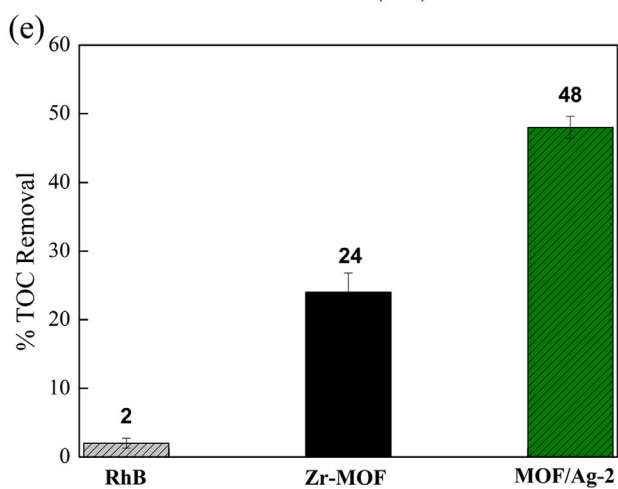
to aromatic compounds, where the absorption band of the RhB (at 554 nm) decreases due to chromophore cleavage and the N-deethylation processes, and then oxidized to ring-opening products and organic acids. Finally, these small molecular intermediates are mineralized into $\rm CO_2$ and $\rm H_2O$ or remain in solution, being the main contributors to the carbon content, as evidenced by the TOC measurements.

Considering the high levels of conversion to CO₂, for the MOF/Ag-2 catalyst under visible radiation for 60 min, only seven intermediates were identified (see **Figure 5**) using a hybrid qTOF/MS analyzer (see Figure S6, Supporting Information









Adv. Sustainable Syst. 2025, e01297

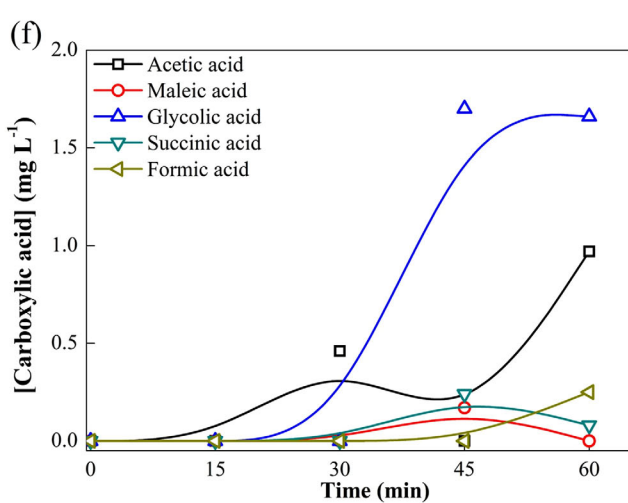


Figure 4. Overall RhB removal performance of all samples a), the corresponding kinetic fitting b), RhB degradation cycles using MOF/Ag-2 c), scavengers species on the photodegradation process (AO = ammonium oxalate, BQ = benzoquinone, TBA = tert-butyl alcohol) d), TOC removal efficiency e), and concentration evolution of the main detected short-chain carboxylic acids as a function of treatment time for the photocatalytic degradation of RhB by MOF/Ag-2 f).

23667486. 0, Downloaded from https://advanced.onlinelibrary.wiley.com/doi/10.1002/adsu202501297 by University Of Sao Paulo - Brazil, Wiley Online Library on [24/11/2025]. See the Terms and Conditions (https://advanced.onlinelibrary.wiley.com/doi/10.1002/adsu202501297 by University Of Sao Paulo - Brazil, Wiley Online Library on [24/11/2025]. See the Terms and Conditions (https://advanced.onlinelibrary.wiley.com/doi/10.1002/adsu202501297 by University Of Sao Paulo - Brazil, Wiley Online Library on [24/11/2025]. See the Terms and Conditions (https://advanced.onlinelibrary.wiley.com/doi/10.1002/adsu202501297 by University Of Sao Paulo - Brazil, Wiley Online Library on [24/11/2025]. See the Terms and Conditions (https://advanced.onlinelibrary.wiley.com/doi/10.1002/adsu202501297 by University Of Sao Paulo - Brazil, Wiley Online Library on [24/11/2025]. See the Terms and Conditions (https://advanced.onlinelibrary.wiley.com/doi/10.1002/adsu202501297 by University Of Sao Paulo - Brazil, Wiley Online Library on [24/11/2025]. See the Terms and Conditions (https://advanced.onlinelibrary.wiley.com/doi/10.1002/adsu202501297 by University Of Sao Paulo - Brazil, Wiley Online Library on [24/11/2025]. See the Terms and Conditions (https://adsu202501297 by University Of Sao Paulo - Brazil, Wiley Online Library on [24/11/2025]. See the Terms and Conditions (https://adsu202501297 by University Of Sao Paulo - Brazil, Wiley Online Library on [24/11/2025]. See the Terms and Conditions (https://adsu202501297 by University Of Sao Paulo - Brazil, Wiley Online Library on [24/11/2025]. See the Terms and Conditions (https://adsu202501297 by University Of Sao Paulo - Brazil, Wiley Online Library on [24/11/2025]. See the Terms and Conditions (https://adsu202501297 by University Of Sao Paulo - Brazil, Wiley Online Library on [24/11/2025]. See the Terms and Conditions (https://adsu202501297 by University Of Sao Paulo - Brazil, Wiley Online Library on [24/11/2025]. See the Terms and Conditions (https://adsu202501297 by University Of Sao Paulo -

ions) on Wiley Online Library for rules of use; OA articles are governed by the applicable Creative Commons



Figure 5. Proposed degradation pathways of RhB by MOF/Ag-2 under visible-light irradiation based on the intermediates as identified by liquid-chromatography coupled to high-resolution mass spectrometry.

and-conditions) on Wiley Online Library for rules of use; OA articles are governed by the applicable Creative Commons

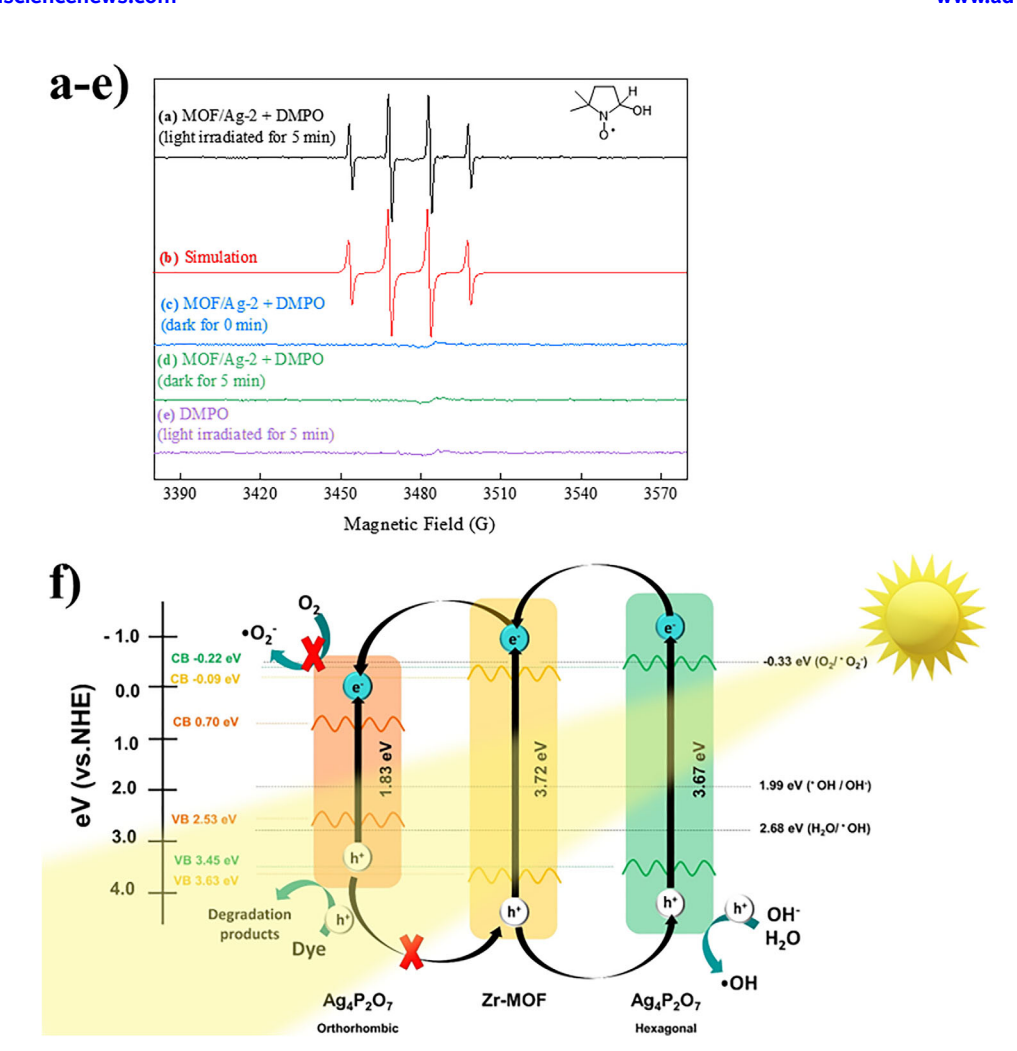


Figure 6. a) EPR spin-trapping spectra of MOF/Ag-2 + DMPO under visible-light irradiation (t = 5 min) showing \bullet OH radical formation. b) Fitted spectrum of the DMPO/ \bullet OH adduct (inset: chemical structure) with hyperfine coupling constants $a_N = 14.85$ G, $a_H{}^{\beta} = 14.98$, and g = 2.0036. c) Control experiment: MOF/Ag-2 + DMPO in the dark (t = 0 min). d) Control experiment: MOF/Ag-2 + DMPO in the dark (t = 0 min). e) Control experiment: DMPO solution under visible-light irradiation (t = 0 min, without catalyst). f) Schematic illustration of the proposed photocatalytic mechanism of the Zr-MOF/Ag₄P₂O₇ heterostructure under visible-light, showing the role of both hexagonal and orthorhombic Ag₄P₂O₇ phases.

for the MS spectra of intermediates). Figure 5 shows the proposed degradation route, in which the RhB oxidation (probably governed by the h^+ and •OH reactive species) is initiated by the successive N-deethylation process followed by oxidized to short-chain byproducts, resulting in products with m/z 415.2028, 387.1709, 359.1401, 331.1084, 165.0197, and 121.0299.

To assess the versatility of MOF/Ag-2, its photocatalytic performance was also evaluated for methylene blue (MB) and methyl orange (MO) under visible-light (Figure S7, Supporting Information). MOF/Ag-2 achieved 96% MB degradation in 10 min, 3.9 times faster than Zr-MOF, with a rate constant of 0.1057 min⁻¹, compared to 0.0364 min⁻¹ for RhB, likely due to structural and functional group differences between dyes (Figure S8, Supporting Information).

Conversely, degradation of the anionic dye MO was modest: 27% after 60 min for MOF/Ag-2 versus 7% for Zr-MOF, following pseudo-first-order kinetics ($k = 1.6 \times 10^{-3} \, \mathrm{min^{-1}}$, Figure S9, Supporting Information). The pronounced selectivity toward cationic dyes (RhB⁺, MB⁺) is attributed to favorable electrostatic interac-

tions. Notably, Zr-MOF synthesized with acetic acid improved MO $^-$ adsorption but reduced MB $^+$ uptake, likely due to altered surface charge from charge-compensation between $\rm Zr_6O_4(OH)_4$ clusters and terephthalate linkers. $^{[72]}$

2.3.2. Photocatalytic Mechanism: Evidence from EPR and Band Structure Analysis

The generation of reactive oxygen species (ROS) during photocatalysis was investigated using Electron Paramagnetic Resonance (EPR) with DMPO (150 mm) as the spin-trapping agent in aqueous suspension. As shown in Figure 6a, MOF/Ag-2 exhibited a characteristic signal attributed to the DMPO/*OH adduct, confirming the formation of hydroxyl radicals (*OH) under visible-light irradiation. Control experiments demonstrated that *OH was exclusively detected under light exposure, evidencing the photoinduced origin of these species. This observation aligns with the scavenger tests (Figure 4d), where the

and-conditions) on Wiley Online Library for rules of use; OA articles are governed by the applicable Creative Commons

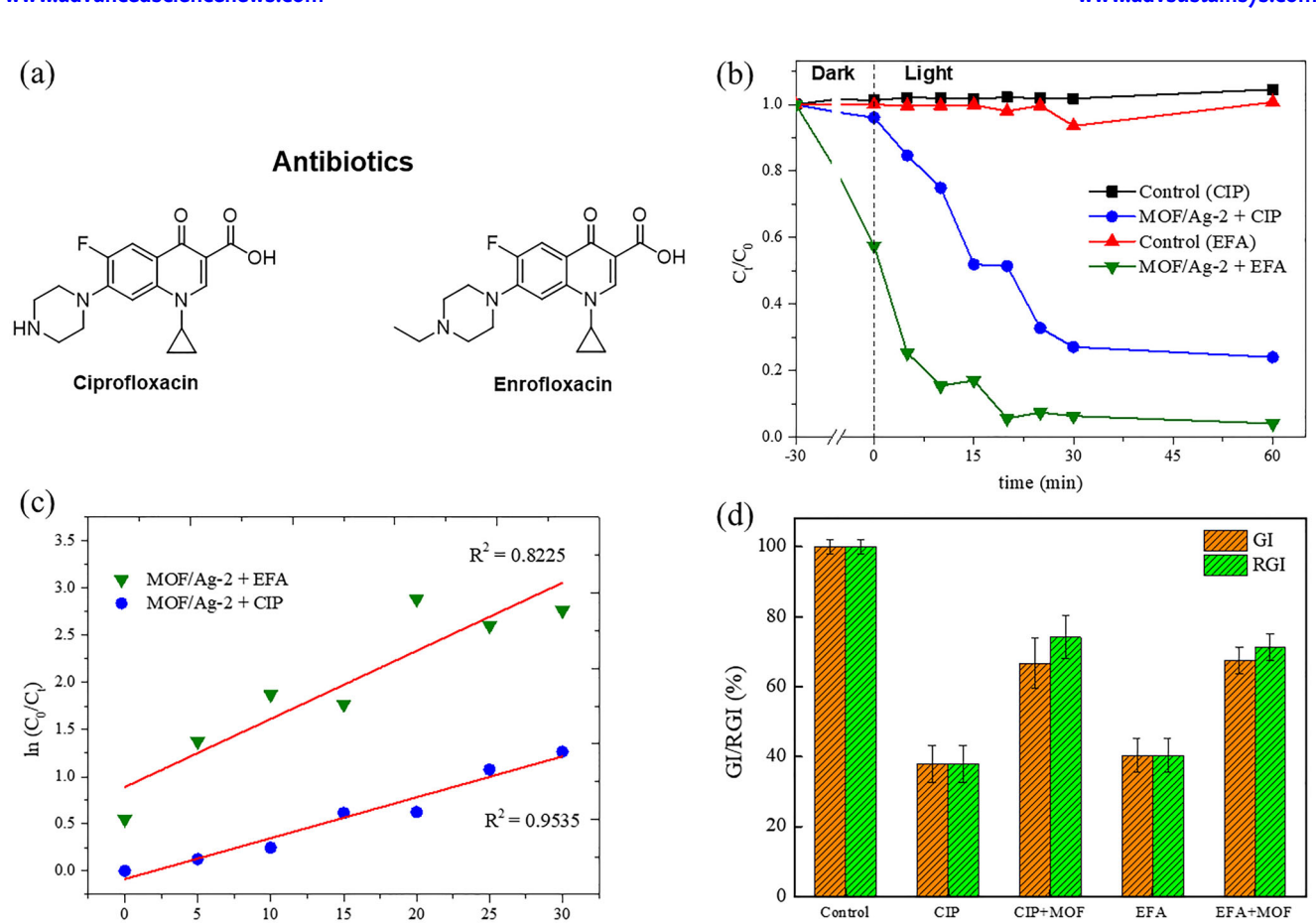


Figure 7. a) Molecular structure of the antibiotics ciprofloxacin and enrofloxacin, b) Photocatalytic curves for degradation of EFA and CIP antibiotics obtained by LC-MS. c) Kinetic curves of EFA and CIP degradation. d) The germination (GI) and relative growth index (RGI) for L. sativa against Control (distilled water), CIP (20 ppm), CIP+MOF, EFA (20 ppm), and EFA+MOF solutions.

presence of TBA, a selective *OH quencher, significantly suppressed RhB degradation, reinforcing the central role of *OH radicals in the photocatalytic process.

time (min)

To elucidate the charge transfer behavior within the heterostructure, the conduction band (CB) and valence band (VB) edge potentials of Zr-MOF and $Ag_4P_2O_7$ were estimated using Mulliken's electronegativity theory (Equations 1 and 2).^[74]

$$E_{VR} = \chi - E_e + 0.5E_\sigma \tag{1}$$

$$E_{CB} = E_{VB} - E_{\sigma} \tag{2}$$

where χ is the electronegativity of the semiconductor and E_e is the energy of free electrons versus hydrogen (4.5 eV). [75] For the Ag₄P₂O₇ sample, the value of $\chi=6.12^{[76]}$ and $E_e=4.5$ eV. As the Ag₄P₂O₇ sample had two E_g , referring to the two phases present in the sample, the E_{g1} and E_{g2} were used for the calculations of CB and VB of the hexagonal and orthorhombic phases, respectively. Thus, using the E_{g1} value of 3.67 eV and Equations (1) and (2), were obtained the values of 3.45 and -0.22 eV for E_{VB} and E_{CB} , respectively. For the E_{g2} value (1.83 eV) the values obtained for E_{VB} and E_{CB} were 2.53 and 0.70 eV, respectively. The CB of Zr-MOF is reported in the literature as

-0.09 eV (vs NHE)^[64] so using equation 2 and $E_{\rm g}=3.72 \text{ eV}$ (see Figure 4e) we can estimate the VB value as being 3.63 eV. On the basis of the Mulliken's theory and EPR result (Figure 6a-e), we proposed that a type II heterostructure forms between both materials, Figure 6f In the proposed mechanism (Figure 6f), under visible-light irradiation, both Zr-MOF and the two polymorphic phases of Ag₄P₂O₇ (hexagonal and orthorhombic) are photoexcited, generating electron-hole (e- - h+) pairs. Owing to the slightly more negative conduction band (CB) potential of Ag₄P₂O₇ (hex) (-0.22 eV) compared with that of Zr-MOF (-0.09 eV) and Ag₄P₂O₇ (ortho) (+0.70 eV), photogenerated electrons flow sequentially from the CB of $Ag_4P_2O_7$ hex) \rightarrow CB of $Zr\text{-MOF} \rightarrow CB \text{ of } Ag_4P_2O_7 \text{ (ortho)}$. This stepwise migration is facilitated by the phase-junction between the Ag₄P₂O₇ polymorphs and by the interfacial heterojunction with Zr-MOF, resulting in efficient spatial separation of charge carriers. The electrons accumulated on the CB of Ag₄P₂O₇ (ortho) are unable to reduce O_2 to $\bullet O_2^-$ directly, since their potential (0.70 eV) is less negative than that of $O_2/\bullet O_2^-$ (-0.33 eV). Meanwhile, the photogenerated holes migrate in the opposite direction-from the valence band (VB) of $Ag_4P_2O_7$ (ortho) (2.53 eV) toward the more positive VB of Zr-MOF (3.63 eV) and $Ag_4P_2O_7$ (hex) (3.45 eV). These h⁺ species in the VB of Ag₄P₂O₇ (hex) possess sufficient oxidative potential

) on Wiley Online Library for rules of use; OA articles are governed by the applicable Creative Commons

to oxidize RhB molecules directly and to produce \bullet OH radicals, since their VB energy (3.45 eV) exceeds the redox potentials of $H_2O/\bullet OH$ (2.68 eV) and $\bullet OH/OH^-$ (1.99 eV). Overall, the synergistic effect of this stepwise type-II band alignment, combining both phase-junction ($Ag_4P_2O_7$ —hex $\leftrightarrow Ag_4P_2O_7$ —ortho) and heterojunction ($Ag_4P_2O_7 \leftrightarrow Zr$ -MOF) interactions, together with the experimental evidence from EPR spectroscopy and radical scavenger assays, demonstrates that the Zr-MOF/ $Ag_4P_2O_7$ heterostructure effectively promotes charge separation and robust ROS generation, leading to superior photocatalytic degradation of cationic dyes and antibiotics in aqueous media.

2.3.3. Photodegradation of Ciprofloxacin and Enrofloxacin Antibiotics by LC-MS, and Phytoxicity Tests of Their Byproducts

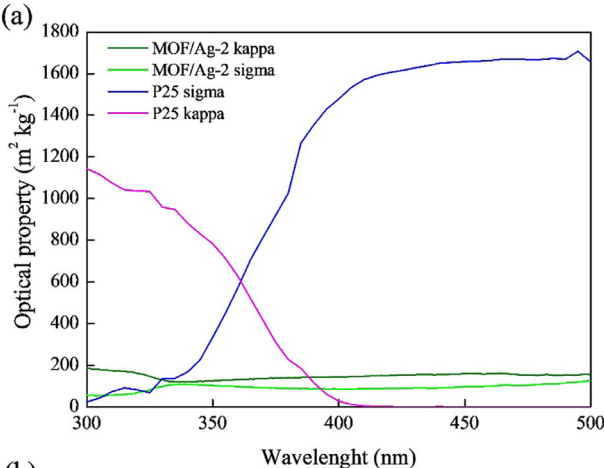
Figure 7a shows the structure of the antibiotics ciprofloxacin (CIP) and enrofloxacin (EFA). The degradation of the CIP and EFA (**Figure 8b**,c) under visible-light irradiation was used as well to assess the photocatalytic performance of MOF/Ag-2 and was evaluated by liquid chromatography-mass spectrometry (LC–MS).

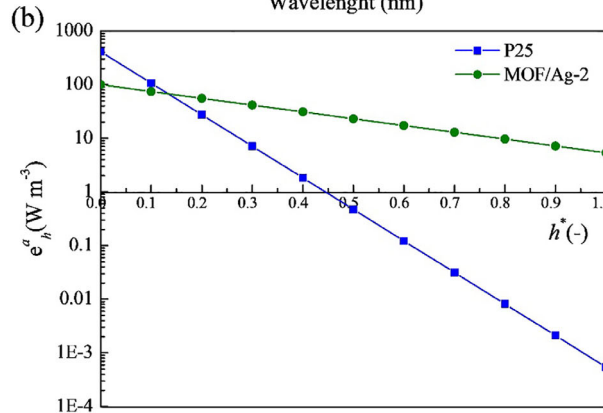
As shown in Figure 7a,b, no significant degradation of CIP and EFA was observed in the control experiments performed without the photocatalyst, indicating that direct photolysis of these antibiotics under visible-light is negligible under the applied experimental conditions. In contrast, the MOF/Ag-2 heterostructure achieved removal efficiencies of \approx 95% for EFA and 75% for CIP within 60 min of photocatalytic treatment (Figure 8b).

These results are particularly promising when compared to other Ag-based photocatalysts reported in the literature. For instance, Ag/AgVO₃/g-C₃N₄ and ZnO/Ag/Ag₃PO₄ composites achieved CIP removal efficiencies of 82.6% and 87.1%, respectively, after 120 min under visible-light irradiation, [77,78] while cocoon-like Ag₃PO₄ showed 97.2% degradation in 30 min.^[79] Regarding EFA, Ag-containing materials such as 3D Ag-ZnFe₂O₄/reduced graphene oxide and Ag₂O/CeO₂ achieved removal efficiencies of 98.7% and 87.1% within 30 and 120 min, respectively.[80,81] Although Zr-based MOFs are widely recognized for their high surface area and tunable functionalities, their application in antibiotic removal-particularly under visible-light remains relatively unexplored. Notably, the amine-functionalized derivative UiO-66-NH2 has been extensively studied due to its improved visible-light absorption capacity.[82,83] In this context, the results obtained here demonstrate that modifying Zr-MOFs with Ag-containing semiconductors is a promising strategy for the effective degradation of persistent organic pollutants, including dyes and pharmaceutical residues, in aquatic environments.

CIP and EFA photodegradation processes were fitted using a pseudo-first-order kinetic model (Figure 7b): $\ln (C_t/C_0) = -kt$, where C_0 and C_t are the concentrations of the antibiotics at the initial state (t = 0) and at each given time t, respectively. The degradation rate constants (k) were 0.043 and 0.0722 \min^{-1} for CIP and EFA, respectively. The higher k obtained for the photodegradation of EFA can be better understood after investigating the bimolecular reaction rate constant of ${}^{\bullet}$ OH ($k_{{}^{\bullet}$ OH) with these two antibiotics.[84]

The results obtained from EPR spectroscopy (Figure 6a) provide compelling evidence for the generation of hydroxyl radicals





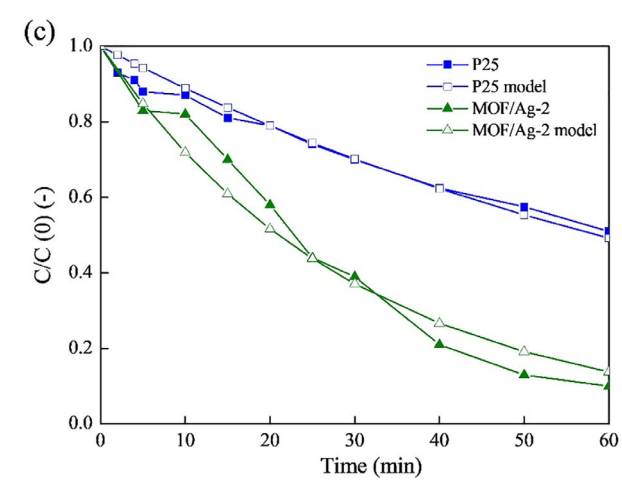


Figure 8. a) Comparison of specific absorption and scattering coefficients for MOF/Ag-2 and the referent TiO_2 photocatalyst, b) Trends of calculated local volumetric photon absorption along the reactor depth, and c) Comparison of model and experimental data for dye degradation using MOF/Ag-2 and TiO_2 P25.

(*OH) by the MOF/Ag-2 composite under visible-light irradiation. The detection of the characteristic DMPO/*OH signal exclusively under irradiation conditions confirms that *OH formation is a photoinduced process. This observation is further corroborated by scavenger experiments (Figure 4d), in which the



www.advsustainsys.com

Table 2. Calculated values of model parameters.

Photocatalyst	$k_{\rm int}$, $10^{-3} W^{-0.5} m^{1.5} min^{-1}$	$e^{\mathrm{a}}_{\mathrm{LUMP}}$, W m $^{-3}$	$P_{\rm ph}^{\rm vis}$, W ${\rm m}^{-3}$	$ au_{app}$		
				UVA [350–400 nm]	Visible I [400–410 nm]	Visible II [430-440 nm]
MOF/Ag-2	2.15	32.10	210	2.920	3.018	3.183
TiO ₂ P25		30.25	_	13.536	21.845	23.258

addition of TBA, a selective OH quencher, markedly suppressed the degradation of RhB. Together, these findings validate the central role of *OH radicals as the dominant oxidative species in the photocatalytic mechanism of MOF/Ag-2. To rationalize the ROS generation mechanism, the electronic band structures of Zr-MOF and Ag₄P₂O₇ were evaluated based on UV-vis data and Mulliken's theory. The analysis revealed the formation of a type II heterojunction between the two semiconductors (Figure 6b), enabling efficient spatial separation of photogenerated electrons and holes. The valence band (VB) of Ag₄P₂O₇ (3.45 eV) lies at a more positive potential than the oxidation thresholds of $H_2O/^{\bullet}OH$ (2.68 eV) and $OH^-/^{\bullet}OH$ (1.99 eV), making the generation of *OH thermodynamically favorable. This alignment supports a mechanism in which holes in the VB of Ag₄P₂O₇ oxidize water or hydroxide ions to form hydroxyl radicals, while electrons are effectively transferred across the heterojunction, minimizing recombination. This mechanistic insight is particularly relevant when interpreting the degradation profiles of CIP and EFA, as presented in Figure 7b. The kinetic data demonstrate a higher degradation rate for EFA compared to CIP, which can be directly linked to their differing reactivities toward hydroxyl radicals. According to literature data. [84] The second-order rate constant for the reaction between *OH and EFA is higher than that for CIP, indicating that EFA undergoes faster oxidation under •OH-dominated conditions. This agrees with our experimental observations and further confirms that *OH radicals are the key species driving the photocatalytic degradation of both antibiotics. In summary, the EPR data, band structure modeling, and photocatalytic performance strongly supports a *OHmediated degradation mechanism facilitated by a type II heterojunction. The system not only ensures efficient charge separation but also promotes robust ROS generation, leading to effective degradation of persistent pharmaceuticals in aqueous media.

Phytotoxicity assays are essential in photocatalytic studies to evaluate the potential formation of toxic byproducts. The toxicity of CIP, EFA, and their degraded solutions (CIP+MOF and EFA+MOF) was assessed via germination index (GI) and relative growth index (RGI) of Lactuca sativa roots (Figure 7d). Lactuca sativa was selected because it is a sensitive and widely used bioindicator species, with rapid germination and easily measurable root growth, allowing reliable assessment of toxicity. [85] Pure CIP and EFA (20 ppm) inhibited seed germination, yielding GI and RGI values ≈40%. In contrast, photodegraded solutions using MOF/Ag-2 exhibited increased GI and RGI (≈70%), suggesting reduced toxicity and effective detoxification. This improvement supports that no harmful intermediates were formed during photocatalysis. The slight reduction in germination compared to the control may stem from residual silver species, known to affect root development by interacting with plant

biomolecules.[86] Overall, MOF/Ag-2 demonstrated strong potential for practical applications, showing high degradation efficiency and stability in dye and antibiotic systems, with phytotoxicity results confirming environmental safety under laboratory conditions.

2.3.4. Photocatalytic Activity Based on Optical Properties

The detailed kinetic model was developed to quantify the contribution of UVA and visible-light to the photocatalytic degradation of selected dyes and antibiotics. The quantification of photocatalytic activity showed the advantageous activity of MOF/Ag-2 compared to the reference photocatalyst TiO₂ P25. Calculated values of model parameters are reported in Table 2. A comparison of optical properties, rates of photon absorption, kinetic models, and experimental results for both TiO2 P25 and MOF/Ag-2 are shown in Figure 8a-c. The obtained values for e^{a}_{LUMP} in UVA are almost the same for both photocatalysts, which can be explained by different portions of scattering and absorption coefficient (Figure 8a). That resulted in different trends of local ea values along the reactor depth (Figure 8b). The same net value of $e^{a}_{LUMP,\;UVA}$ was obtained due to the hydrodynamic properties of the reaction system where lump parameters were observed.

To better explain the influence of optical properties on the photocatalytic activity, the apparent optical thickness ($\tau_{\rm app}$) was calculated for each photocatalyst in the wavelength range that corresponds to the emitted irradiation (Figure S3, Supporting Information), Equation (3).

$$\tau_{app} = a\tau \sqrt{1 - \omega_{corr}^2} \tag{3}$$

Note that ω_{corr} stands for the corrected scattering albedo, au is the optical thickness, and a is the SFM model parameter.[38] Calculated τ_{ann} values are shown in Table 2.

Notably, apparent optical thickness (Table 2) is higher for TiO₂ P25 in all studied wavelength ranges, while corresponding values for MOF/Ag-2 remained low. Lower τ_{app} values mean that the photocatalyst is optically more transparent to incident irradiation. These findings favor further study of such novel photocatalysts, as they showed better overall activity and better intrinsic photocatalytic properties. The results obtained by the applied model correspond well to the experimental results (Figure 8c). The model term $P_{\rm ph}^{\rm vis}$ is the overall photon absorption rate in visible-light that can be further expanded and used to study the exact intrinsic properties of novel photocatalysts in different parts of visible irradiation. In the current study, $P_{\rm ph}^{\ \ \rm vis}$ was 210, almost seven times higher than the lump photon absorption in UVA

www.advsustainsys.com

(32.10), showing the potential of using the MOF/Ag-2 catalyst under solar irradiation.

The kinetic modeling developed in this work, although initially applied to the degradation of the cationic dye Rhodamine B, has a generalizable character to other organic compounds, such as dyes and pharmaceuticals, as long as they share photochemical mechanisms based on the generation of reactive oxygen species (ROS). The confirmation of the predominant formation of the hydroxyl radical (*OH) through EPR analysis in aqueous medium corroborates this extrapolation, since *OH is a highly reactive and poorly selective species, capable of promoting the degradation of a wide range of organic compounds. Additionally, since the kinetic model considers intrinsic parameters of the system, such as photon absorption ($P_{\rm ph}^{\rm vis}$), apparent optical thickness ($\tau_{\rm app}$), and local distribution of radiant energy in the reactor, its applicability is not restricted to a specific pollutant, but rather to the physicochemical conditions of the process. However, it is necessary to consider that variations in the substrate affinity with the catalyst surface, regulated by factors such as zeta potential and electrostatic interactions, can impact the overall efficiency of the process. Therefore, the extrapolation of data to other dyes and drugs is valid, especially for molecules susceptible to oxidation by ROS, as long as complementary analyses are performed on the adsorption stage and possible diffusion barriers in the system.

3. Conclusion

This study demonstrates that Zr-MOF, Ag₄P₂O₇, and their heterostructured composites can be rapidly assembled via a microwave-assisted strategy, yielding structurally integrated photocatalysts with enhanced solar responsiveness. Comprehensive structural and optical analyses confirmed the formation of a welldefined heterojunction in the MOF/Ag-2 sample, enabling efficient charge-carrier separation and superior photon utilization. The material exhibited remarkable colloidal stability and surface characteristics, which synergistically promoted pollutant adsorption and photocatalytic turnover. As a result, MOF/Ag-2 delivered outstanding degradation efficiencies toward organic dyes and fluoroquinolone antibiotics, with LC-MS and phytotoxicity assays validating the transformation of pollutants into less harmful intermediates. Mechanistic insights from EPR and scavenger studies identified •OH radicals and photogenerated holes as the dominant species, providing a clear understanding of the photocatalytic pathways. Although the band-edge positions were estimated by Mulliken's electronegativity approach, future studies involving Mott-Schottky, XPS, and impedance analyses would be valuable to experimentally confirm the electronic band alignment and charge-transfer behavior of the Zr-MOF/Ag₄P₂O₇ heterostructures. In addition, the coexistence of two Ag₄P₂O₇ phases (hexagonal and orthorhombic) may form phase junctions that facilitate charge separation and reactive species generation. Altogether, this work highlights Zr-MOF/Ag₄P₂O₇ as a rationally engineered, solar-driven platform for sustainable pollutant degradation. Beyond wastewater remediation, the design principles outlined here establish a blueprint for next-generation multifunctional photocatalysts that unite structural robustness, solar energy harvesting, and environmental compatibility, advancing the development of sustainable systems for global environmental challenges.

4. Experimental Section

Zr-based MOFs and $Ag_4P_2O_7$ were synthesized by a microwave-assisted solvothermal route. The heterostructured MOF/ $Ag_4P_2O_7$ composites were obtained by combining Zr-MOF with silver and phosphate precursors under controlled conditions (160 °C, 64 min). The structural, morphological, and optical properties of the synthesized materials were characterized by X-ray diffraction (XRD), Fourier-transform infrared spectroscopy (FT-IR), scanning (SEM) and transmission (TEM) electron microscopy, UV-vis diffuse reflectance spectroscopy (UV-vis DRS), and photoluminescence (PL) spectroscopy. Hydrodynamic size and surface charge were assessed by dynamic light scattering (DLS) and zeta potential analyses.

The photocatalytic activity was evaluated under visible-light irradiation for the degradation of Rhodamine B (RhB), Methylene Blue (MB), and Methyl Orange (MO) dyes, as well as the antibiotics ciprofloxacin (CIP) and enrofloxacin (EFA). EPR spectroscopy and radical scavenger experiments identified the reactive species involved in the degradation mechanism. LC-MS and phytotoxicity assays (*Lactuca sativa*) confirmed the formation of less toxic by-products. A kinetic model incorporating Six-Flux Modeling (SFM) was applied to quantify photon absorption and photocatalytic rates.

Full experimental details, synthesis procedures, instrumentation settings, and kinetic equations are provided in (\$1-\$1.10, Supporting Information).

Supporting Information

Supporting Information is available from the Wiley Online Library or from the author.

Acknowledgements

This study was financed in part by the Conselho Nacional de Desenvolvimento Científico e Tecnológico – CNPq (163342/2020-2) and Coordenação de Aperfeiçoamento de Pessoal de Nível Superior - Brasil (CAPES) - Finance Code 001. This study was financed, in part, by the São Paulo Research Foundation (FAPESP), Brasil (#2013/07296-2, #2023/08525-7, #2019/22183-6, #2021/14394-7, #2021/13985-1 and #2025/09383-7), Shell and the strategic importance of the support given by ANP (Brazil's National Oil, Natural Gas and Biofuels Agency) through the R&D Levy regulation and the Humboldt Foundation for his fellowship.

The Article Processing Charge for the publication of this research was funded by the Coordenacao de Aperfeicoamento de Pessoal de Nivel Superior - Brasil (CAPES) (ROR identifier: 00x0ma614).

Conflict of Interest

The authors declare no conflict of interest.

Data Availability Statement

The data that support the findings of this study are available from the corresponding author upon reasonable request.

Keywords

antibiotics, Ciprofloxacin, emerging contaminants, Enrofloxacin, metalorganic frameworks, sustainable remediation, visible-light photocatalysis, $Zr\text{-MOF/Ag}_4P_2O_7$ heterostructure

Received: September 17, 2025 Revised: October 26, 2025 Published online:

23667486, 0, Downloaded from https

onlinelibrary.wiley.com/doi/10.1002/adsu.202501297 by University Of Sao Paulo

Brazil, Wiley Online Library on [24/11/2025]. See

the Terms

Library for rules of use; OA articles are governed by the applicable Creative Con

SCIENCE NEWS

www.advsustainsys.com

- F. M. D. Chequer, G. A. R. de Oliveira, E. R. A. Ferraz, J. Carvalho, M. V. Boldrin Zanoni, D. P. de Oliveira, *Text. Dyes: Process Environ. Impact* 2013, 10, 53659.
- [2] G. N. Iwuoha, A. Akinseye, Nigeria. Chem. Inter. 2019, 5, 198.
- [3] E. B. Hassen, A. M. Asmare, Chem. Inter. 2019, 5, 87.
- [4] A. Z. B. Kaouthar Djehaf, R. Ouhib, H. Benmansour, A. Bentouaf, A. Mahdad, N. Moulay, D. Bensaid, M. Ameri, Chem. Inter. 2017, 3, 414.
- [5] I. T. Carvalho, L. Santos, Environ. Int. 2016, 94, 736.
- [6] M. S. de Ilurdoz, J. J. Sadhwani, J. V. Reboso, J. Water Process Eng. 2022, 45, 102474.
- [7] I. M. C. Gonçalves, A. Gomes, R. Brás, M. I. A. Ferra, M. T. P. Amorim, R. S. Porter, *JSDC* 2000, 116, 393.
- [8] N. K. Amin, Desalination 2008, 223, 152.
- [9] I. Uzun, Dyes Pigm. 2006, 70, 76.
- [10] A. Ajmal, I. Majeed, R. N. Malik, H. Idrissc, M. A. Nadeem, RSC Adv. 2014. 4, 37003.
- [11] M. A. Kazi, Pak. J. Anal. Environ. Chem. 2019, 20, 135.
- [12] E. S. Elmolla, M. Chaudhuri, Desalination 2010, 252, 46.
- [13] L. G. da Trindade, L. Zanchet, A. B. Trench, J. C. Souza, M. H. Carvalho, A. J. A. de Oliveira, E. C. Pereira, T. M. Mazzo, E. Longo, *Ionics* 2018, 25, 3197.
- [14] S. Chavoshan, M. Khodadadi, N. Nasseh, J. Environ. Health. Sci. Engineer 2020, 18, 107.
- [15] S. Nahar, M. R. Hasan, A. A. H. Kadhum, H. A. Hasan, M. F. M. Zain, J. Photochem. Photobiol. A: Chem. 2019, 375, 191.
- [16] S. Li, B. Xue, J. Chen, Y. Liu, J. Zhang, H. Wang, J. Liu, Sep. Purif. Technol. 2021, 254, 117579.
- [17] A. B. Trench, T. R. Machado, A. F. Gouveia, C. C. Foggi, V. Teodoro, I. Sánchez-Montes, M. M. Teixeira, L. G. da Trindade, N. Jacomaci, A. Perrin, C. Perrin, J. M. Aquino, J. Andrés, E. Longo, ACS Omega 2020, 5, 23808.
- [18] Y. Wang, H. Yang, X. Sun, H. Zhang, T. Xian, Mater. Res. Bull. 2020, 124, 110754.
- [19] L. Di, H. Yang, T. Xian, X. Chen, Nanoscale Res. Lett. 2018, 13, 257.
- [20] Q. H. Tran, V. Q. Nguyen, A. T. Le, Adv. Nat. Sci.: Nanosci. Nanotechnol. 2018, 9, 049501.
- [21] H. Furukawa, K. E. Cordova, M. O'Keeffe, O. M. Yaghi, Science 2013, 341, 1230444.
- [22] P. Deria, J. E. Mondloch, O. Karagiaridi, W. Bury, J. T. Hupp, O. K. Farha, Chem. Soc. Rev. 2014, 43, 5896.
- [23] J. Ding, Z. Yang, C. He, X. Tong, Y. Li, X. Niu, H. Zhang, J. Colloid Interface Sci. 2017, 497, 126.
- [24] L. G. da Trindade, K. M. N. Borba, A. B. Trench, L. Zanchet, V. Teodoro, F. M. L. Pontes, E. Longo, T. M. Mazzo, J. Solid State Chem. 2021, 293, 121794.
- [25] S. Gao, T. Feng, C. Feng, N. Shang, C. Wang, J. Colloid Interface Sci. 2016, 466, 284.
- [26] H. Wang, X. Yuan, Y. Wu, G. Zeng, H. Dong, X. Chen, L. Leng, Z. Wu, L. Peng, Appl. Catal. B 2016, 186, 19.
- [27] Y. Dong, H. Zhang, F. Lei, M. Liang, X. Qian, P. Shen, H. Xu, Z. Chen, J. Gao, J. Yao, J. Solid State Chem. 2017, 245, 160.
- [28] J. F. Blandez, A. Santiago-Portillo, S. Navalón, M. Giménez-Marqués, M. Álvaro, P. Horcajada, H. García, J. Mol. Catal. A Chem. 2016, 425, 332
- [29] A. Wang, H. Liang, F. Chen, X. Tian, S. Jing, P. Tsiakaras, Chemosphere 2022, 307, 135699.
- [30] Q. Wang, Q. Gao, A. M. Al-Enizi, A. Nafady, S. Ma, *Inorg. Chem. Front.* 2020, 7, 300.
- [31] N. Liu, J. Zhang, Y. Wang, Q. Zhu, C. Wang, X. Zhang, J. Duan, B. Hou, J. Sheng, Colloids Surf. A: Physicochem. Eng. Asp. 2022, 664, 128813.
- [32] A. Arenas-Vivo, S. Rojas, I. Ocaña, A. Torres, M. Liras, F. Salles, D. Arenas-Esteban, S. Bals, D. Ávila, P. Horcajada, J. Mater. Chem. A 2021, 9, 15704.

- [33] X. Lin, R. Liu, W. Nie, F. Tian, X. Liu, Environ. Sci. Pollut. Res. 2024, 31, 2394.
- [34] X. Zheng, R. Han, X. Jiang, J. Mei, Y. Gao, J. Yang, Y. Li, S. Cui, Chemosphere 2022, 305, 135352.
- [35] N. Liu, J. Zhang, Y. Wang, Q. Zhu, X. Zhang, J. Duan, B. Hou, *Nanomaterials* 2022, 12, 1946.
- [36] I. Grčić, G. L. Puma, Appl. Catal. B 2017, 211, 222.
- [37] M. Plodinec, I. Grčić, M. G. Willinger, A. Hammud, X. Huang, I. Panžić, A. Gajović, J. Alloys Compd. 2019, 776, 883.
- [38] I. Grčić, G. L. Puma, Environ. Sci. Technol. 2013, 47, 13702.
- [39] N. Zhang, X. Zhang, C. Gan, J. Zhang, Y. Liu, M. Zhou, C. Zhang, Y. Fang, J. Photochem. Photobiol. A: Chem. 2019, 376, 305.
- [40] H. Koizumi, T. Hirono, T. Yamada, Y. Miyamoto, N. Ogawa, M. Koizumi, M. Shimada, Mater. Res. Bull. 1986, 21, 817.
- [41] T. Yamada, H. Koizumi, J. Cryst. Growth 1983, 64, 558.
- [42] Y. Q. Yi Luan, Z. Jin, X. Peng, H. Gao, G. Wang, RSC Adv. 2015, 5, 19273.
- [43] S. A. Suthanthiraraj, R. Sarumathi, Appl. Nanosci. 2012, 3, 501.
- [44] H. Brintzinger, R. A. Plane, Inorg. Chem. 1967, 6, 623.
- [45] W. S. da Pereira, C. B. Gozzo, E. Longo, E. R. Leite, J. C. Sczancoski, Appl. Surf. Sci. 2019, 493, 1195.
- [46] Y. Maréchal, J. Mol. Struc. 2011, 004, 146.
- [47] W. S. Pereira, C. B. Gozzo, E. Longo, E. R. Leite, J. C. Sczancoski, Appl. Surf. Sci. 2019, 493, 1195.
- [48] S. Promnopas, W. Promnopas, W. Maisang, S. Wannapop, T. Thongtem, S. Thongtem, O. Wiranwetchayan, Sci. Rep. 2023, 13, 4742.
- [49] S. A. Suthanthiraraj, R. Sarumathi, Appl. Nanosci. 2013, 3, 501.
- [50] G. Botelho, J. Andres, L. Gracia, L. S. Matos, E. Longo, ChemPlusChem 2016, 81, 202.
- [51] V. Guillerm, F. Ragon, M. Dan-Hardi, T. Devic, M. Vishnuvarthan, B. Campo, A. Vimont, G. Clet, Q. Yang, G. Maurin, G. Férey, A. Vittadini, S. Gross, C. Serre, *Angew. Chem. Int.* 2012, 51, 9267.
- [52] G. Férey, C. Serre, Chem. Soc. Rev. 2009, 38, 1380.
- [53] Y. Bai, Y. Dou, L. Xie, W. Rutledge, J. Li, H. C. Zhou, Chem. Soc. Rev. 2016, 45, 2327.
- [54] C. Duan, Y. Yu, J. Xiao, X. Zhang, L. Li, P. Yang, J. Wu, H. Xi, Sci. China Mater. 2020, 63, 667.
- [55] Z. Zhao, Y. Zhang, S. Y. Song, H. J. Zhang, Coord. Chem. Rev. 2019, 398, 113007.
- [56] B. A. Gibbons, E. M. Johnson, M. K. Javed, X. Yang, A. J. Morris, ACS Appl. Mater. Interfaces 2024, 16, 52703.
- [57] M. Y. Tsang, A. Sinelshchikova, O. Zaremba, F. Schöfbeck, A. D. Balsa, M. R. Reithofer, S. Wuttke, J. M. Chin, Adv. Funct. Mater. 2024, 34, 2308376.
- [58] F. Zhu, Q. Chai, D. Xiong, N. Zhu, J. Zhou, R. Wu, Z. Zhang, Biosensors 2024, 14, 273.
- [59] Y. Li, Z. Tang, C. Chen, Crystals 2021, 11, 434.
- [60] H. Furukawa, F. Gándara, Y. B. Zhang, J. J. Jiang, W. L. Queen, M. R. Hudson, O. M. Yaghi, J. Am. Chem. Soc. 2014, 136, 4369.
- [61] C. Rosales-Martínez, D. López-Alcalá, M. Assis, C. Castillo-Blas, J. J. Baldoví, I. A. Lázaro, RSC Adv. 2024, 14, 37984.
- [62] C. Rosales-Martínez, M. Assis, C. Castillo-Blas, I. A. Lázaro, Chem. Commun. 2024, 60, 8280.
- [63] D. L. Wood, J. Tauc, Phys. Rev. B 1972, 5, 3144.
- [64] A. Wang, Y. Zhou, Z. Wang, M. Chen, L. Sun, X. Liu, RSC Adv. 2016, 6, 3671.
- [65] V. Ramasubbu, P. R. Kumar, E. M. Mothi, K. Karuppasamy, H. S. Kim, T. Maiyalagan, X. S. Shajan, Appl. Surf. Sci. 2019, 496, 143646.
- [66] C. X. Li, R. Wang, W. Sun, K. Cui, X. Z. Fu, M. Cui, Y. Chen, Z. Guo, Y. Liu, J. Environ. Chem. Eng. 2024, 12, 113288.
- [67] N. Guettaï, H. A. Amar, Desalination 2005, 185, 439.
- [68] N. L. Gavade, A. N. Kadam, Y. B. Gaikwad, M. J. Dhanavade, K. M. Garadkar, J. Mater. Sci. Mater. Electron. 2016, 27, 11080.

www.advsustainsys.com

- [69] S. Wang, Y. Jia, L. Song, H. Zhang, ACS Omega 2018, 3, 18456.
- [70] Z. He, S. Yang, Y. Ju, C. Sun, J. Environ. Sci. 2009, 21, 268.
- [71] S. Singh, S. L. Lo, Environ. Sci. Pollut. Res. 2018, 25, 6532.
- [72] J. Qiu, Y. Feng, X. Zhang, M. Jia, J. Yao, J. Colloid Interface Sci. 2017, 499, 151.
- [73] G. R. Buettner, Free Radical Biol. Med. 1987, 3, 259.
- [74] Y. Xu, M. A. A. Schoonen, Am. Min. 2000, 85, 543.
- [75] J. Tian, P. Hao, N. Wei, H. Cui, H. Liu, ACS Catal. 2015, 5, 4530.
- [76] Y. Dian, C. Zhi-Da, W. Fan, L. Shu-Zhou, Acta Phys. -Chim. Sin 2001, 17, 15.
- [77] M. F. R. Samsudin, C. Frebillot, Y. Kaddoury, S. Sufian, W.-J. Ong, J. Environ. Manage. 2020, 270, 110803.
- [78] C. Du, J. Song, S. Tan, L. Yang, G. Yu, H. Chen, L. Zhou, Z. Zhang, Y. Zhang, Y. Su, X. Wen, S. Wang, Mater. Chem. Phys. 2021, 260,

- [79] J. Li, L. Jin, F. Liu, X. Liu, Mater. Lett. 2019, 242, 139.
- [80] K. Wang, S. Zhan, D. Zhang, H. Sun, X. Jin, J. Wang, RSC Adv. 2021, 11, 4723.
- [81] X. J. Wen, C. G. Niu, L. Zhang, C. Liang, G. M. Zeng, Appl. Catal. 2018, 221, 701.
- [82] Q. Su, J. Li, B. Wang, Y. Li, L. Hou, Appl. Catal. 2022, 318, 121820.
- [83] C. Zhao, Y. Li, H. Chu, X. Pan, L. Ling, P. Wang, H. Fu, C. C. Wang, Z. Wang, J. Hazard. Mater. 2021, 419, 126466.
- [84] L. Ge, G. Na, S. Zhang, K. Li, P. Zhang, H. Ren, Z. Yao, Sci. Total Environ. 2015, 12, 527.
- [85] A. A. Rodrigues, D. A. Rodrigues, J. F. Sales, S. C. Vasconcelos Filho, A. C. Costa, C. L. Rodrigues, A. A. da Silva, M. Domingos, C. Müller, Plants 2022, 11, 3406.
- [86] F. Mirzajani, H. Askari, S. Hamzelou, M. Farzaneh, A. Ghassempour, Ecotoxicol. Environ. Saf. 2013, 88, 48.

Adv. Sustainable Syst. 2025, e01297